

Atomistic calculations of the electronic, thermal, and thermoelectric properties of ultra-thin Si layers

Neophytos Neophytou · Hossein Karamitaheri ·
Hans Kosina

Published online: 19 November 2013
© Springer Science+Business Media New York 2013

Abstract Low-dimensional semiconductors are considered promising candidates for thermoelectric applications with enhanced performance because of a drastic reduction in their thermal conductivity, κ_l , and possibilities of enhanced power factors. This is also the case for traditionally poor thermoelectric materials such as silicon. This work presents atomistic simulations for the electronic, thermal, and thermoelectric properties of ultra-thin Si layers of thicknesses below 10 nm. The Linearized Boltzmann theory is coupled: (i) to the atomistic $sp^3d^5s^*$ tight-binding (TB) model for the electronic properties of the thin layers, and (ii) to the modified valence-force-field method (MVFF) for the calculation of the thermal conductivity of the thin layers. We calculate the room temperature electrical conductivity, Seebeck coefficient, power factor, thermal conductivity, and ZT figure of merit of ultra-thin p-type Si layers (UTLs). We describe the numerical formulation of coupling TB and MVFF to the linearized Boltzmann transport formalism. The properties of UTLs are highly anisotropic, and optimized thermoelectric

properties can be achieved by the choice of the appropriate transport and confinement orientations, as well as layer thickness.

Keywords Thermoelectrics · Tight-binding · $sp^3d^5s^*$ · Modified valence-force-field · Boltzmann transport · Seebeck coefficient · Thermoelectric power factor · Silicon ultra-thin layers · ZT figure of merit

1 Introduction

Low-dimensional semiconductor nanostructures are promising candidates for next generation thermoelectric (TE) applications because of their extremely low thermal conductivities compared to those of their corresponding bulk material. This is the case even for traditionally poor thermoelectric materials such as Si, which has recently received significant attention in the thermoelectric community. The ability of a material to convert heat into electricity is measured by the dimensionless figure of merit $ZT = \sigma S^2 T / (\kappa_e + \kappa_l)$, where σ is the electrical conductivity, S is the Seebeck coefficient, and κ_e and κ_l are the electronic and lattice parts of the thermal conductivity, respectively. Silicon, the most common semiconductor with the most advanced industrial processes, is a poor TE material with room temperature $ZT_{bulk} \sim 0.01$, a result of its high thermal conductivity $\kappa_l \sim 140$ W/mK. Si nanostructures, on the other hand, have demonstrated a significantly higher $ZT \sim 0.5$ [1–4], and they are now considered as emerging candidates for high efficiency and large volume production TE applications [5].

This large performance improvement was a result of a drastic reduction in the Si nanostructures' thermal conductivity to values down to $\kappa_l = 1\text{--}2$ W/mK, close to the amorphous limit. Additionally, benefits to the ZT figure of merit

N. Neophytou (✉) · H. Karamitaheri · H. Kosina
Institute for Microelectronics, TU Wien,
Gußhausstraße 27-29/E360, 1040 Wien, Austria
e-mail: neophytou@iue.tuwien.ac.at

H. Karamitaheri
e-mail: karami@iue.tuwien.ac.at

H. Kosina
e-mail: kosina@iue.tuwien.ac.at

H. Karamitaheri
Department of Electrical Engineering, University of Kashan,
Kashan 87317-51167, Iran

N. Neophytou
School of Engineering, University of Warwick, Coventry,
CV4 7AL, UK

can come from the power factor σS^2 as well. By nanostructuring, the electronic structure could be engineered to tune the Seebeck coefficient [6–8] and the electrical conductivity independently [9], which could maximize σS^2 . For example, Hicks and Dresselhaus suggested that the sharp features in the low-dimensional density of states function $\text{DOS}(E)$ can improve the Seebeck coefficient [6, 7]. Mahan and Sofo have further shown that thermoelectric energy conversion through a single energy level (0D channel) can reach the Carnot efficiency when κ_l is zero [10].

For a proper optimization of the thermoelectric properties in low-dimensional channels, electronic and phononic bandstructure models that fully consider the atomistic nature of the channels over large length scales need to be employed in order to guide the design of such devices. For example, in Refs. [11–13] we described in detail a computational model based on the atomistic $\text{sp}^3\text{d}^5\text{s}^*$ -spin-orbit-coupled ($\text{sp}^3\text{d}^5\text{s}^*$ -SO) tight-binding (TB) model [14–18] and Linearized Boltzmann transport for calculations of the thermoelectric power factor of ultra-narrow Si NWs. In those works, we pointed out that the power factor of low-dimensional channels can be optimized by appropriately choosing the transport orientation and confinement length scale such that high conductivity is achieved, despite a mild reduction in the Seebeck coefficient. In Ref. [19] we described a model based on the atomistic modified valence-force-field method (MVFF) and the Landauer transport approach for the calculation of the thermal conductivity of ultra-narrow Si NWs. In this work, we extend these formalisms to investigate the thermoelectric properties of 2D ultra-narrow Si thin layers (UTLs) from fully atomistic perspective. The $\text{sp}^3\text{d}^5\text{s}^*$ TB model and the MVFF method are coupled to linearized Boltzmann transport for the calculation of the electronic and thermal properties of the UTLs, respectively. The numerical methodologies and the approximations used are described. We present results on p-type UTLs that demonstrate the largest anisotropy in their transport properties, and for which the atomistic modeling approach is more appropriate due to the complications of the warped bands, as we showed in Refs. [20, 21], although the method we consider is generic for both n-type and p-type UTLs. We finally extract the ZT figure of merit in the UTLs, showing that room temperature values of $ZT \sim 0.5$ can indeed be achieved, in agreement with experimental data in Si nanostructures.

The paper is organized as follows: In Sect. 2 we describe the calculation of the electronic properties of the UTLs and in Sect. 3 the calculation of their thermal properties. In Sect. 4 we compute the ZT figure of merit. Finally, Sect. 5 summarizes and concludes the work.

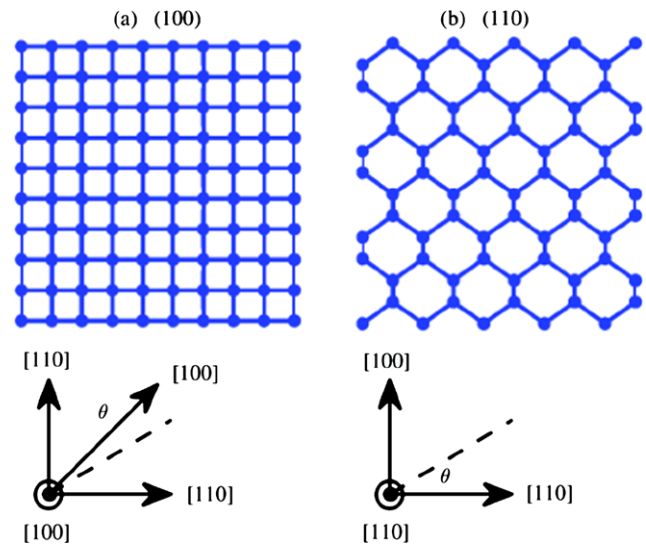


Fig. 1 The atomistic structure of the cross sections of the (a) (100) and (b) (110) silicon ultra-thin layer surfaces. In both cases the x -axis is along the [110] transport direction. Arbitrary transport orientations can be considered by varying the angle θ between 0 and π

2 Calculation of the electronic properties of Si 2D UTLs

The UTL bandstructure is calculated using the 20 orbital atomistic tight-binding $\text{sp}^3\text{d}^5\text{s}^*$ -spin-orbit-coupled model [14, 17, 20], which is sufficiently accurate and inherently includes the effects of different transport and quantization orientations. We consider infinitely long, uniform, silicon UTLs on the (100) and (110) surface orientations. The transport orientation considered is the [110] as shown in Fig. 1. By considering these two surfaces we demonstrate the strong anisotropy of the transport properties. The surfaces are assumed to be passivated. The passivation technique details are provided in Refs. [13, 22].

We perform full band calculations by coupling TB bandstructure to linearized Boltzmann transport theory [11, 23]. The electrical conductivity σ and the Seebeck coefficient S are computed as:

$$\sigma = q_0^2 \int_{E_V}^{\infty} dE \left(-\frac{\partial f_0}{\partial E} \right) \mathcal{E}(E), \quad (1a)$$

$$S = \frac{q_0 k_B}{\sigma} \int_{E_V}^{\infty} dE \left(-\frac{\partial f_0}{\partial E} \right) \mathcal{E}(E) \left(\frac{E - E_F}{k_B T} \right), \quad (1b)$$

where the transport distribution function $\mathcal{E}(E)$ is defined as [24]:

$$\begin{aligned} \mathcal{E}(E) &= \frac{1}{W} \sum_{k_x, y, n} v_n^2(k_x) \tau_n(k_x, y) \delta(E - E_n(k_x, y)) \\ &= \frac{1}{W} \sum_n v_{k_x, n}^2(E) \tau_n(E) g_{2D}^n(E). \end{aligned} \quad (2)$$

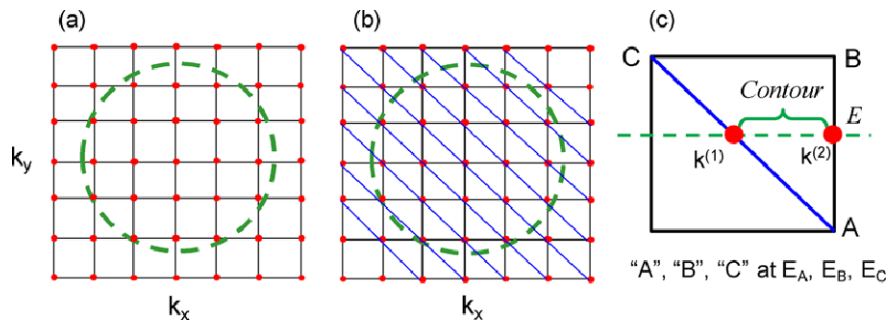


Fig. 2 The simulation procedure for the extraction of the density of states versus energy. (a) The k -space rectangular grid used for the bandstructure calculation with a sample contour (dashed green).

(b) The rectangular grid is separated into triangles. (c) An individual triangle whose three corners are placed in between energy E (Color figure online)

Here $v_{k_x,n}(E) = \frac{1}{\hbar} \frac{\partial E_n}{\partial k_x}$ is the group velocity in the transport direction, $\tau_n(k_{x,y})$ is the momentum relaxation time of a carrier with in-plane wave number $k_{x,y}$ in subband n , $g_{2D}^n(E_n)$ is the density of states for a 2D subband, E_V is the valence band edge, W is the thickness of the channel, and E_F is the Fermi level, determined by the doping of the material. The mobility μ can also be extracted from $\mu = \frac{\sigma}{q_0 p}$, where p is the carrier concentration in the channel. In the calculations, we actually use the Fermi level as an input parameter, and for a certain Fermi level, the carrier density (assumed to be equal to the doping density) is extracted.

Extraction of the $g_{2D}(E)$ An essential numerical point in the calculation of the electronic properties, is the calculation of the density of states (DOS) of the subbands of the 2D channel at a certain energy, $g_{2D}^n(E_n)$. Since we consider a numerical/arbitrary bandstructure calculated in k -space, in order to use it within the Linearized Boltzmann formalism, the k -space-dependent DOS needs to be converted into an energy-dependent function to be used within the $\mathcal{E}(E)$ function of Eq. (2). For this we use the following scheme presented in Fig. 2. We compute the electronic structure on a rectangular k_x – k_y grid as shown in Fig. 2a. The available eigen-energies are, therefore, available at the k -grid points. The energy contour at a specific energy E then needs to be computed (i.e. dashed green line). Once the energy contour is known, the DOS at the corresponding energy of the particular subband can be computed as:

$$g_{2D}^n(E) = \int_{C_k} \langle v_n(k_x, k_y, E) \rangle dk, \quad (3)$$

where $\langle v_n(k_x, k_y, E) \rangle$ is the average group velocity of the states in subband n at energy E along the contour C_k computed as $v_n(k_x, k_y, E) = \sqrt{v_n(k_x, E)^2 + v_n(k_y, E)^2}$, where each component of the directional velocities is given by $v_n(k_{x/y}, E) = \frac{1}{\hbar} \frac{\partial E_n(k_{x/y})}{\partial k_{x/y}}$, where $E_n(k_{x/y})$ is the energy of the particular state in subband n .

For illustration regarding the contour extraction we consider a circular contour in the k_x – k_y space as shown in

Fig. 2a, although the approach works for arbitrary contour shapes. To construct the contour of a subband at a specific energy, the following steps are performed: (i) We divide the rectangular k -space grid into triangles as shown in Fig. 2b and keep record the coordinates and the energies E_A , E_B , and E_C of the three triangle corners as shown in Fig. 2c. (ii) We find the eigen-energies of the specific subband into consideration that reside around the energy of interest (within a lower and upper energy cutoffs) and record the triangles which have the energy of one of their corners above/below and the energies of the other two corners below/above that energy level. This indicates that the energy contour passes through that triangle as shown in Fig. 2c. (iii) The third step is to compute the k -space length of the contour segments in each of the relevant triangles. This is done by simple geometric considerations. The $k_{x,y}$ -points on the triangle sides at energy E (the red labeled dots $k^{(1)}/k^{(2)}$ in Fig. 2c) are given by:

$$k_{x/y}^{(1/2)} = k_{x/y}^A + (k_{x/y}^{B/C} - k_{x/y}^A) \frac{(E - E^A)}{(E_{x/y}^{B/C} - E_{x/y}^A)} \quad (4)$$

The length of the individual segments is then computed as:

$$dk^{(1 \rightarrow 2)} = \sqrt{(k_x^{(1)} - k_x^{(2)})^2 + (k_y^{(1)} - k_y^{(2)})^2} \quad (5)$$

Once the individual segment lengths dk are extracted, the energy resolved density of states is computed using Eq. (3). Note that for the velocity $\langle v_n(k_x, k_y, E) \rangle$ we use the average of the velocities of the bandstructure at the three points of their corresponding triangle.

Figures 3a and 3b show typical examples for the energy contours in p-type Si UTLs of thicknesses $W = 3$ nm on the (100) and (110) surfaces, respectively. Contours at various different energies are shown, indicating that the method correctly captures essential bandstructure features such as warping and anisotropy, as we presented in Ref. [20]. The differences between the contours of the two surfaces indicate the importance of the anisotropy of the material at the

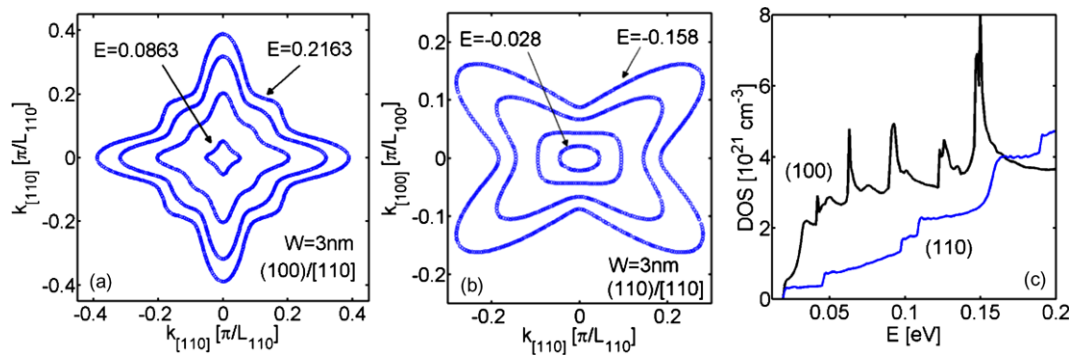


Fig. 3 (a) Energy contours of the first subband of the p-type (100)/[110] UTL of $W = 3$ nm. (b) Energy contours of the first subband of the p-type (110)/[110] UTL of $W = 3$ nm. (c) The density of

states versus energy of the (100) (black) and the (110) (blue) surfaces of (a) and (b), respectively (Color figure online)

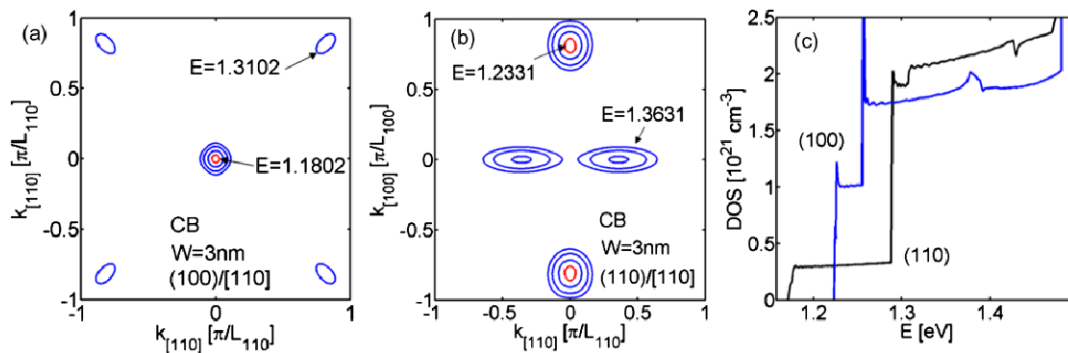


Fig. 4 (a) Energy contours of the first subband of the n-type (100)/[110] UTL of $W = 3$ nm. (b) Energy contours of the first subband of the n-type (110)/[110] UTL of $W = 3$ nm. (c) The density of

states versus energy of the (100) (black) and the (110) (blue) surfaces of (a) and (b), respectively. Red contours belong to the lowest energy valleys (see energy values) (Color figure online)

nanoscale, and point to the fact that the choice of different surfaces will result in different transport properties. The energy resolved density of states $\text{DOS}(E)$ for the two surfaces is shown in Fig. 3c. The $\text{DOS}(E)$ is lower for the (110) surface (blue line), an indication of the lighter effective mass of this channel and the superior transport properties also addressed in detail in Refs. [20, 21]. The deviations from the flat plateaus in the $\text{DOS}(E)$ point to the non-parabolicity of the bands, whereas the discontinuities point to the onsets of the different subbands. Figures 4a and 4b show the same quantities for the corresponding n-type channels on the (100) and (110) surfaces, respectively. The projections of the six ellipsoids on the 2D k -space are captured as expected and the onset of the different subbands and valleys is also captured in the $\text{DOS}(E)$ plot of Fig. 3c. Note that for the rest of the paper only the (110)/[110] and (100)/[110] p-type channels are considered. p-Type channels are the ones addressed less frequently due to the difficulty in describing their bandstructure. Furthermore, the p-type (110) surface has superior transport properties compared to the other surfaces, e.g. compared to the (100) surface [20, 21, 25], and can serve as an example in optimizing the properties of channels at the nanoscale. For example, experimental work

on the mobility of MOSFET devices by Yang *et al.* [25], showed that the (110)/[110] p-type channel has the highest low-field mobility at inversion conditions compared to all differently oriented channels. This was also demonstrated specifically for thin layers by Tsutsui *et al.* in Ref. [26]. In both cases, the mobility was almost $2\times$ higher compared to the mobility of the (100) surface channels. Our simulation work in Ref. [21], showed that indeed this channel has superior transport properties, i.e. the mobility is higher than that of differently oriented channels, but in addition, it increases as the (110) layer thickness is decreased as the bands become lighter with confinement and the carriers acquire higher velocities [20]. This was not the case for channels on different surfaces. Importantly, Ref. [21], also showed that this channel is only weakly sensitive to surface roughness scattering due to its high confinement effective mass (as we demonstrate below), which makes it very suitable for ultra-thin-layer devices.

Relaxation rates and approximations After the extraction of the density of states, Fermi's Golden rule is used to extract the momentum relaxation rates. We include scattering due to elastic acoustic phonons (ADP), inelastic opti-

cal phonons (ODP), and surface roughness (SRS), and use the full energy dependence for the momentum relaxation times as shown in Fig. 5. This figure shows a schematic of elastic (red-dashed arrows) and inelastic (blue-solid arrows) processes, indicating that all bandstructure shape details are considered in the extraction of the relaxation times. Note that we consider acoustic phonon scattering as an elastic process, although in principle there is a small energy associated with such transitions. This, however, only has an impact at low temperatures. At room temperature, which is what is considered in this work, since the thermal energy is larger than the corresponding phonon energy, the elastic acoustic phonon scattering treatment is adequate. For computational efficiency, we make the following approximations, also commonly employed in numerical calculations: (i) Confinement of phonons is neglected, and dispersionless bulk phonons are assumed. Instead, enhanced deformation potential values $D_{\text{ODP}}^{\text{holes}} = 13.24 \times 10^{10}$ eV/m and $D_{\text{ADP}}^{\text{holes}} = 5.34$ eV are employed in order to capture the effect of enhanced phonon scattering due to modifications in the phonon spectrum. This is common practice for nanostructures throughout the literature [23, 27–30]. These values are usually calibrated to mobility measurements on 2D channels, and good accuracy is achieved. This is possible because

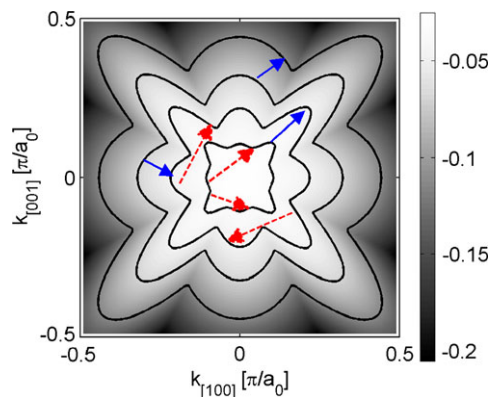
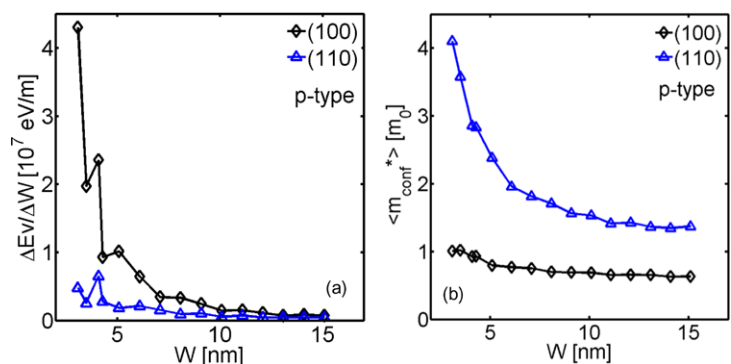


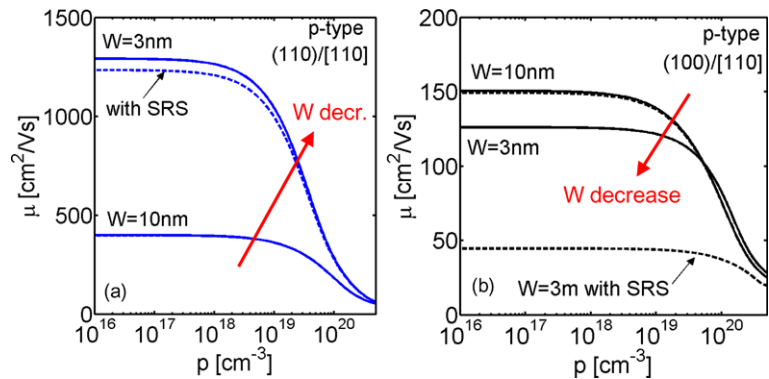
Fig. 5 An example of scattering processes on a typical p-type bandstructure. Elastic transitions (red-dashed arrows) and inelastic transitions (blue-solid arrows) are indicated (Color figure online)

Fig. 6 (a) Change in band edges as a function of film thickness. Results for UTLs of (100) (diamond-black), and (110) (triangle-blue) surface orientations are shown. (b) The average confinement effective mass for the UTLs of (a). This is calculated from the change in the subband edges with confinement using the particle in a box quantization picture (Color figure online)



confined phonons have only quantitative effect on charge transport, as pointed out by the calculations of Donetti *et al.* [31]. Their influence can be lumped into an enhanced deformation potential amplitude. For example, studies on the effect of confined phonons on the phonon-limited mobility of p-type thin layers [31], as well as GaAs NWs [32] have also shown that the influence of phonon confinement is rather weak. The influence of acoustic phonon confinement can be somewhat more important on the phonon limited mobility of ultra-narrow nanowires, but even in that case it is only of the order of ~ 10 – 20 %, and reduces fast as the diameter is increased [23, 33–35]. Clearly, the presence of additional scattering mechanisms (such as surface roughness scattering) also limits the conductivity, and the effect of phonon confinement on the total conductivity will be even smaller. One additional uncertainty comes from the assumptions about the boundary conditions for phonons used in the calculations. Two types of boundary conditions are usually employed: (a) the free surface boundary conditions (FSBCs), and (b) the clamped/rigid surface boundary conditions (CSBCs). FSBCs tend to increase, whereas CSBCs tend to decrease the scattering rates [33, 34]. The calculated confined acoustic phonon limited mobility can differ depending on the nature of the surfaces assumed. In some cases, the results using bulk acoustic phonons, lie somewhere between the two [34]. (ii) The second approximation is that surface relaxation is neglected. (iii) The third approximation is that for SRS we assume a 2D exponential autocorrelation function for the roughness with $\Delta_{\text{rms}} = 0.48$ nm and $L_C = 1.3$ nm [28] and derive the transition rate from the shift in the band edges $\Delta E_V/\Delta W$ with confinement. As discussed by Uchida *et al.* [36], this is the strongest contribution to SRS in channels of a few nanometers in thickness. In Fig. 6a we show the quantity $\Delta E_V/\Delta W$ for the (110) and (100) surfaces versus the UTL thickness W . Considerable differences are observed between the two surfaces, further indication of the strong anisotropy in their properties. The band edges in the case of the (100) surface (black-diamond line) have a very strong sensitivity to the layer thickness. It implies that channels on this particular surface will be very sensitive and strongly affected by SRS as well. On the other

Fig. 7 Low-field mobility for UTLs of thicknesses $W = 3$ nm and $W = 10$ nm as denoted. Solid lines: phonon-limited mobility. Dashed lines: phonon plus SRS-limited mobility. (a) (110)/[110] channel, (b) (100)/[110] channel (Color figure online)



hand, the band edge of the (110) surface is almost invariant to changes in the layer thickness (blue-triangle line), which indicates that SRS will only affect this surface weakly. Another way to see this is by extracting an effective confinement mass for the valleys of these channels using a simple particle in a box quantization picture. Large confinement mass translates into difficulty in shifting the energy levels with well thickness variation. The effective confinement mass is shown in Fig. 6b for the two channels as a function of the UTL thickness. Indeed, for the (110) surface (blue-triangle line), the effective confinement mass reaches very large values $\sim 4m_0$, whereas in the (100) surface only $\sim m_0$ (black-diamond line).

Finally, we note that in our calculations we employ atomistic description of both electronic and phononic bandstructure (further below), but the calculations are empirical in nature. Empirical parameters are used to calibrate the tight-binding and the modified valence-force-field models to Si bulk dispersions. We assume that since we fit the bulk dispersions in the entire Brillouin zone, the parameters are still transferable to nanostructures. In addition, the validity of both, the tight-binding and the modified valence-force-field models, has been verified through experimental data for nanostructures in various occasions [15, 37].

Mobility Figures 7a and 7b show the calculated mobility for the (110)/[110] and (100)/[110] channels, respectively. In each case we show channels with thicknesses $W = 3$ nm and $W = 10$ nm as denoted in Fig. 7, and for each channel, results for the phonon-limited mobility (solid lines) and the phonon plus SRS-limited mobility (dashed lines). A few observations can be made in this figure: (i) The effect of SRS is very weak for UTLs of thicknesses $W = 10$ nm. The dashed lines and the solid lines in the cases of the $W = 10$ nm UTLs are almost overlapping. (Note that we do not include any electrostatic fields in the calculation that will confine carrier near the surface.) (ii) In the case of the thinner $W = 3$ nm UTLs, SRS is still weak for the (110) channel in Fig. 7a, but is quite strong in the case of the (100) channel (compare the solid $W = 3$ nm line with the dashed $W = 3$ nm line

as denoted in Fig. 7b). In the latter, SRS reduces the mobility by a factor of $\sim 3\times$ compared to the phonon-limited value. (iii) The mobility of the (110) channels is by almost an order of magnitude higher than that of the corresponding (100) channels, especially at low carrier densities. This is attributed to the low effective mass and higher hole velocities on this surface [20]. (iv) The mobility in the (110) channel increases with reducing width. The mobility increases by almost $3\times$ as the layer thickness is reduced from 10 nm to 3 nm. This again is attributed to the reduction of the transport effective mass on the (110) surface, attributed to the warping of the heavy-hole band as we discuss in detail in Refs. [20, 21, 38]. On the other hand, the hole mobility on the (100) surface follows the usual trend, i.e. the mobility reduces with layer thickness. This trend is usually attributed to the enhanced electron-phonon interaction with increasing carrier confinement which increases scattering.

Thermoelectric properties The thermoelectric properties of the thinner $W = 3$ nm channels are shown in Fig. 8. The superior transport properties of the (110) p-type Si channel are evident in its thermoelectric properties. Figures 8a, 8b and 8c show the electrical conductivity, the Seebeck coefficient, and the power factor versus carrier density, respectively. As expected, the conductivity of the (110)/[110] channel (blue lines) in Fig. 8a is considerably higher than that of the (100)/[110] channel (black lines). As also follows from the mobility calculations in Fig. 7, SRS does not affect the conductivity of the (110)/[110] channel (dashed blue line), whereas it significantly reduces the conductivity of the (100)/[110] channel (dashed black line). The Seebeck coefficients follow the reverse trend, namely they decrease with carrier density, with the (100)/[110] channel having the highest values (black lines). SRS helps to slightly increase the Seebeck coefficient of this channel. A comparison between the conductivity and Seebeck coefficient values, however, shows that the conductivity is strongly anisotropic, whereas the Seebeck coefficient is not as much. The reason is that the Seebeck coefficient in nanostructures depends strongly on the distance of the subbands from

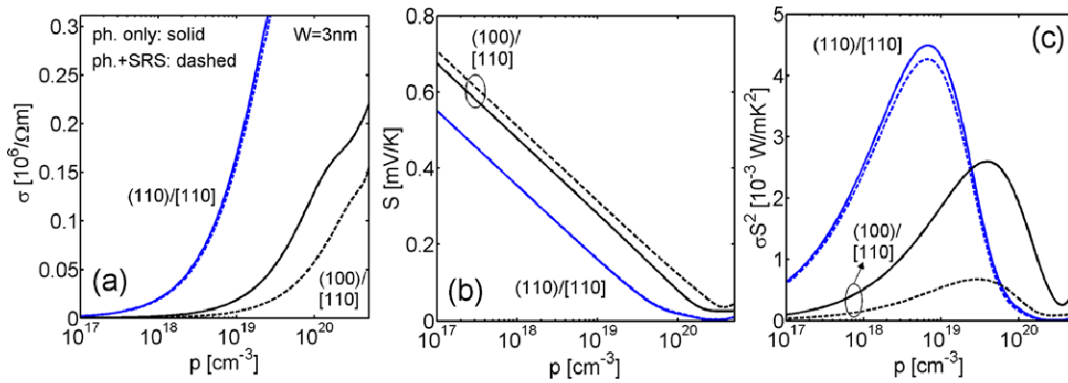


Fig. 8 Thermoelectric coefficients versus carrier concentration for the $W = 3$ nm p-type UTL, in the [110] transport orientation at 300 K. Channels on the (110) and (100) confinement surfaces are shown by the blue and black lines, respectively as denoted in the figures. Two

different carrier scattering situations are considered, (i) phonons (*solid lines*), and (ii) phonons plus SRS (*dashed lines*). (a) The electrical conductivity. (b) The Seebeck coefficient. (c) The power factor (Color figure online)

the Fermi level E_F , and is independent of bandstructure at first order [39]. This difference in the properties of the two channels is evident in their thermoelectric power factors in Fig. 8c. The (110)/[110] channel outperforms the (100)/[110] channel (blue versus black lines). In addition, the power factor of the latter is strongly affected by SRS and further reduced. A crucial point that these results demonstrate is the importance of high conductivity over the Seebeck coefficient in determining the thermoelectric properties of nanoscale materials. Design of the material's bandstructure for achieving high electrical conductivity rather than high Seebeck coefficient, provides larger power factors, despite the initial efforts which focused on achieving high Seebeck coefficients in low-dimensional materials.

3 Calculation of the thermal conductivity of Si 2D UTLs

In order to fully evaluate the thermoelectric properties of the UTLs, we also need to compute their thermal conductivity. In Si, the dominant component of the thermal conductivity originates from the transport of phonons. In this section we calculate the thermal conductivity in Si UTLs using the modified valence-force-field (MVFF) method for the phonon bandstructure calculation, coupled to the phononic Boltzmann transport equation for computing the lattice thermal conductivity.

MVFF method The modified valence-force-field method [40] can accurately capture the bulk Si phonon spectrum as well as the effects of confinement [37]. In this method the inter-atomic potential is modeled by the following bond deformations: bond stretching U_{bs} , bond bending U_{bb} , cross bond stretching U_{bs-bs} , cross bond bending stretching U_{bs-bb} , and coplanar bond bending interactions U_{bb-bb}

Table 1 Force constants for silicon from Ref. [40] (in units of N/m)

	α	β	δ	γ	ν
Si	49.4	4.79	5.2	0	6.99

calculated as:

$$U_{bs}^{ij} = \frac{3}{8} \alpha \frac{(r_{ij}^2 - d_{ij}^2)^2}{d_{ij}^2} \quad (6a)$$

$$U_{bb}^{jik} = \frac{3}{8} \beta \frac{(\Delta\theta_{jik})^2}{d_{ij}d_{ik}} \quad (6b)$$

$$U_{bs-bs}^{jik} = \frac{3}{8} \delta \frac{(r_{ij}^2 - d_{ij}^2)(r_{ik}^2 - d_{ik}^2)}{d_{ij}d_{ik}} \quad (6c)$$

$$U_{bs-bb}^{jik} = \frac{3}{8} \gamma \frac{(r_{ij}^2 - d_{ij}^2)(\Delta\theta_{jik})}{d_{ij}d_{ik}} \quad (6d)$$

$$U_{bb-bb}^{jkl} = \frac{3}{8} \nu \frac{(\Delta\theta_{jik})(\Delta\theta_{ikl})}{\sqrt{d_{ij}d_{ik}^2d_{kl}}} \quad (6e)$$

where \vec{r}_{ij} and \vec{r}_{ij} are equilibrium and non-equilibrium bond vectors from atom 'i' to 'j', respectively, and $\Delta\theta_{jik} = \vec{r}_{ij} \cdot \vec{r}_{iik} - \vec{d}_{ij} \cdot \vec{d}_{iik}$ is the angle deviation of the bonds between atoms 'i' and 'j' and atoms 'i' and 'k' [37]. The force constants α , β , δ , γ , and ν are fitting parameters to match experimental data for bulk silicon dispersion. In our calculations we use the parameters from Ref. [40] as shown in Table 1.

The total potential energy of the system is defined as:

$$U \approx \frac{1}{2} \sum_{i \in N_A} \left[\sum_{j \in nn_i} U_{bs}^{ij} + \sum_{j,k \in nn_i}^{j \neq k} (U_{bb}^{jik} + U_{bs-bs}^{jik} + U_{bs-bb}^{jik}) + \sum_{j,k,l \in COP_i}^{j \neq k \neq l} U_{bb-bb}^{jkl} \right] \quad (7)$$

which is zero when all the atoms are located in their equilibrium positions. Here, N_A , nn_i , and COP_i are the number of atoms in the system, the number of the nearest neighbors of a specific atom ‘ i ’, and the coplanar atom groups for atom ‘ i ’, respectively [37]. If only two atoms ‘ i ’ and ‘ j ’ slightly move away from their equilibrium positions along m and n axes ($m, n \in [x, y, z]$), respectively, the total potential energy increases to U_{mn}^{ij} . Under the harmonic approximation, the corresponding element of dynamic matrix is then calculated as:

$$D_{mn}^{ij} = \frac{\partial^2 U_{mn}^{ij}}{\partial r_m^i \partial r_n^j} \quad (8)$$

and the dynamic matrix tensor between atoms ‘ i ’ and ‘ j ’ is given by [37]:

$$D_{ij} = \begin{bmatrix} D_{xx}^{ij} & D_{xy}^{ij} & D_{xz}^{ij} \\ D_{yx}^{ij} & D_{yy}^{ij} & D_{yz}^{ij} \\ D_{zx}^{ij} & D_{zy}^{ij} & D_{zz}^{ij} \end{bmatrix} \quad (9)$$

Finally, the dynamic matrix is set up as:

$$D = [D_{3 \times 3}^{ij}] = \begin{bmatrix} \frac{1}{M} \left\{ \begin{array}{ll} D_{ij} & i \neq j \\ -\sum_{l \neq i} D_{il} & i = j \end{array} \right\} \end{bmatrix} \quad (10)$$

where M is the atomic mass of Si. Afterwards, the following eigenvalue problem is solved to calculate the phononic dispersion:

$$D + \sum_l D_l \exp(i\vec{q} \cdot \vec{\Delta} R_l) - \omega^2(q)I = 0 \quad (11)$$

where D_l is the dynamic matrix representing the interaction between the central unit cell and its neighboring unit cells separated by $\vec{\Delta} R_l$ [41]. The calculated phonon dispersion of bulk silicon along the high symmetry lines of the Brillouin zone is shown in Fig. 9 (solid-blue line). An excellent fit to the experimental data (red dots) taken from Ref. [42] is found. The MVFF method has already been used for computing the phonon dispersion of Si nanowires [19, 37], and in this work we extend this method to describe the phonon properties of UTLs. Figure 10 shows an example for the calculation of the phonon bandstructure of the (110) surface UTL of thickness $W = 3$ nm. The first five of the low energy phonon subbands are shown. The black lines indicate cuts along the [100] and [110] transport orientations through the Γ -point.

The thermal conductivity can then be calculated using the phonon relaxation time approximation in the phononic Boltzmann transport equation as [43]:

$$\kappa_l = k_B \sum_{s,q} v_{g,s}^2(q) |\tau_s(q)| \left[\frac{\hbar \omega_s(q)}{k_B T} \right]^2 \frac{e^{\hbar \omega_s(q)/k_B T}}{(e^{\hbar \omega_s(q)/k_B T} - 1)^2} \quad (12)$$

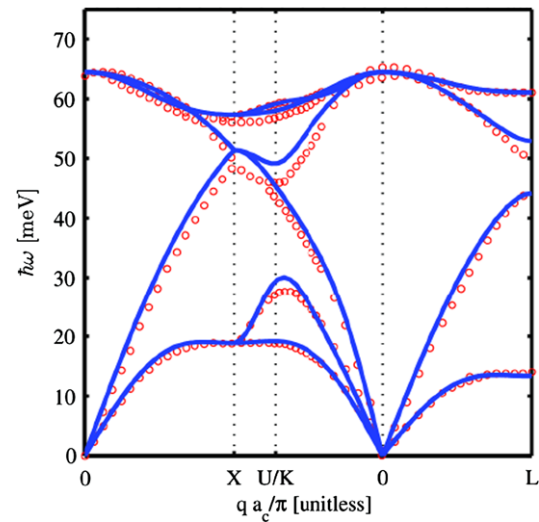


Fig. 9 Phononic bandstructure of bulk silicon (solid blue) in the entire Brillouin zone evaluated using the MVFF method. Experimental results (red circles) are from Ref. [42] (Color figure online)

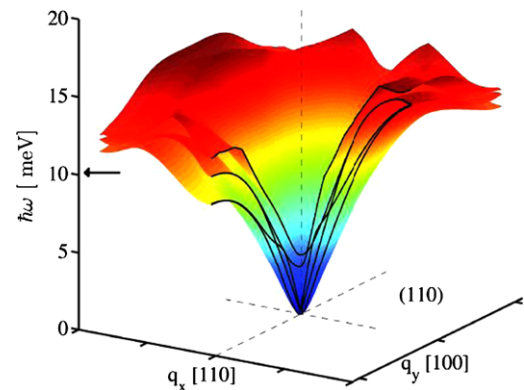


Fig. 10 Part of the phononic band spectrum (5 subbands) of the $W = 3$ nm UTL on the (110) surface. The black lines show the dispersion cuts along the [100] and [110] orientations through the Γ -point (Color figure online)

where k_B is the Boltzmann constant, $v_{g,s}(q)_{||}$ is the transport component of the group velocity of phonons of wavevector q in subband s , and $\tau_s(q)$ is the scattering time. For the calculation of the relaxation times, we follow the bulk formalism for Umklapp scattering:

$$\frac{1}{\tau_U} = B \omega_s(q)^2 T \exp\left(-\frac{C}{T}\right) \quad (13)$$

where $B = 2.8 \times 10^{-19}$ s/K and $C = 140$ K [44]. An important point is that at low frequencies nanostructures have a different phonon density of states from that of bulk materials. Because of this, the bulk scattering model for Umklapp scattering causes divergence in the thermal conductivity, something described by Ziman as “the problem of long longitudinal waves” since the 60 s [45]. To avoid this divergence, Mingo *et al.* proposed to include a second order

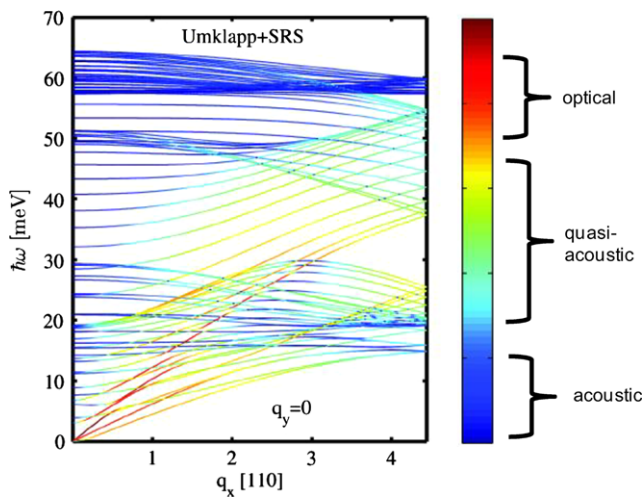


Fig. 11 The phononic dispersion cuts along [110] direction through the Γ -point of the $W = 3$ nm (110) UTL dispersion shown in Fig. 10. The colormap indicates the contribution of each phonon state to the thermal conductivity when Umklapp plus diffusive boundary scattering mechanisms are considered. Three band regions can be identified: (i) The low frequency acoustic modes, (ii) The high frequency optical modes, and (iii) The middle frequency range quasi-acoustic modes, which appear as a result of confinement of the bulk acoustic modes (Color figure online)

3-phonon scattering rate as [46]:

$$\frac{1}{\tau_{U2}} = A_0 T^2 \quad (14)$$

Although this is just an order of magnitude approximation, its consideration can help to remove the singularity for low frequency phonons. We found that $A_0 = 15000 \text{ s}^{-1} \text{ K}^{-2}$ can accurately capture both temperature and diameter dependences of the thermal conductivity of silicon nanowires calibrated against non-equilibrium Green's function calculations from Ref. [47] and molecular dynamics calculations from Ref. [48]. We thus use the same value in this work for UTLs.

For boundary scattering we use:

$$\frac{1}{\tau_{B,s}(q)} = \frac{1 - P}{1 + P} \frac{\bar{v}_{g,s}(q)}{W} \quad (15)$$

where W is the confinement size (UTL thickness) and P is the surface scattering specularity parameter that varies between 0 (for fully diffusive boundary scattering) and 1 (for fully specular boundary scattering). In our calculation we assume that $\bar{v}_{g,s}(q)$ is the average of parallel and perpendicular components of the group velocity, and consider the boundary scattering to be fully diffusive, which is a fairly good estimate for ultra thin UTLs [49]. Finally, the overall relaxation rate is then computed using Matthiessen's rule.

The phonon spectrum consists of several subbands. Figure 11 shows the phononic dispersion cut along the [110] direction through the Γ -point of the bandstructure for the

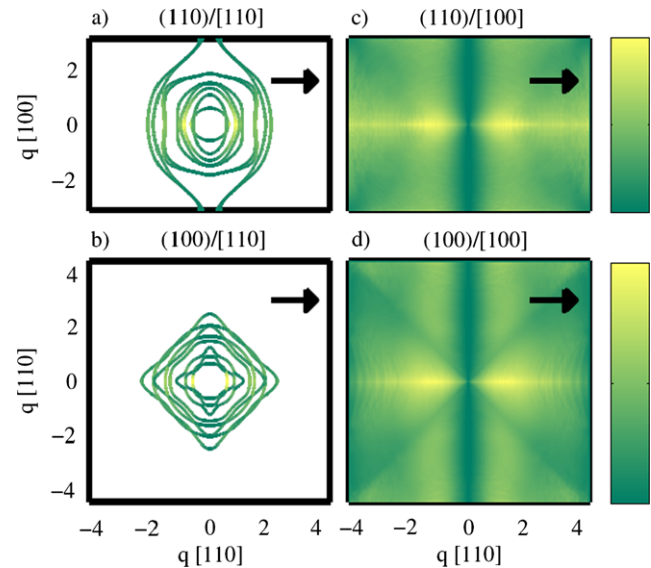
$W = 3$ nm (110) thin layer. The dispersion is somewhat different from the usual acoustic/optical two-band dispersion. The bands can be separated into three categories: (a) the low-frequency acoustic bands, (b) the high frequency optical bands, and (c) the quasi-acoustic modes in the middle region of the frequency range, which originate from the confinement of acoustic modes. Not all of them, however contribute equally to thermal transport. The colormap in Fig. 11 indicates the contribution of each phonon state to the thermal conductivity when considering Umklapp plus boundary scattering limited transport (assuming fully diffusive boundaries). Most of the contribution is attributed to the low frequency, acoustic and quasi-acoustic modes, whereas the contribution of the optical modes is limited due to their small group velocity and short mean-free-paths. Nevertheless, although small, their contribution is increased in proportion to the Umklapp-limited scattering case because boundary scattering reduces the mean-free-path of the acoustic modes, bringing it relatively more close to that of the optical modes. We find, therefore, that in the case of fully diffusive boundary scattering the contribution of the optical modes is considerable (under Umklapp-limited scattering the contribution of the optical phonons is much smaller).

As in the case of electronic transport, phonon transport in Si UTLs is also anisotropic, although at a much lower degree. Recently in Ref. [50] we showed that the ballistic thermal conductance of Si UTLs can vary up to $2\times$ depending on the surface and transport orientations of the channels. The diffusive thermal conductivity of thin layers follows a similar anisotropic trend as well, also originating from the anisotropy in the phonon spectrum. Figure 12 illustrates this point by showing the contributions to the thermal conductivity of the phonon spectrum of the (110)/[110] (Fig. 12a) and (100)/[110] (Fig. 12b) $W = 3$ nm channels at the energy 10 meV (i.e. along a cut in the q_x - q_y spectrum through the arrow shown in the dispersion illustrated in Fig. 10). The phonon dispersions are different on different surfaces, but also along different directions, similarly to the case of the electronic dispersions. The features of the dispersion can provide understanding to the anisotropic behavior of the thermal conductivity in the different layers, although as we show below for these two channels the variation is very small. In general, we note that differently orientated channels could have larger anisotropy in their thermal properties [50]. Figures 12c and 12d show the cumulative thermal conductivity of these channels (when Umklapp and fully diffusive boundary scattering are considered) of all states in the two-dimensional q -space. This figure illustrates the contribution of the different parts of the Brillouin zone to the conductivity of these two channels along the transport direction indicated by the arrows. In both cases, the largest contributions (bright yellow regions) come from the acoustic modes whose group velocity is directed in the transport orientation. The overall thermal conductivity of these

Table 2 Thermal conductivity of Si ultra-thin layers in [W/mK]

Channel description	W = 3 nm (100)/[110]	W = 3 nm (110)/[110]	W = 10 nm (100)/[110]	W = 10 nm (110)/[110]
Umklapp scattering only	40.6	45.3	37.1	43.0
Umklapp + SR scattering	2.6	2.7	6.4	7.3

Fig. 12 Energy contours at $\hbar\omega = 10$ meV of the phonon dispersion of the (a) (110)/[110] and (b) (100)/[110] $W = 3$ nm UTLs in the 2D q_x - q_y space. The color shows the contribution of each phonon state to the thermal conductivity under Umklapp plus diffusive phonon-boundary scattering considerations. (c) and (d) Show the cumulative thermal conductivity as a function of the 2D q -space for the channels in (a) and (b) respectively (bright yellow indicates the highest and dark green the lowest contributions). The transport orientations are indicated by arrows (Color figure online)



two channels is summarized in Table 2. The Umklapp plus boundary scattering limited thermal conductivity is as low as $\kappa_l = 2.7$ W/mK and $\kappa_l = 2.6$ W/mK for the (110)/[110] and (100)/[110] UTLs, respectively. This is a significant reduction from the Umklapp-limited thermal conductivity which is $\kappa_l = 45.3$ W/mK and $\kappa_l = 40.6$ W/mK for the two surfaces, respectively, indicating the importance of the boundary scattering for phonons. This is also a significant reduction from the thermal conductivity of the thicker $W = 10$ nm UTLs which is almost a factor of $3\times$ higher. Note that Umklapp-limited conductivity is at first order thickness independent as shown in Table 2.

4 Calculation of the ZT figure of merit

Once the thermoelectric power factor and the thermal conductivity are calculated, the ZT figure of merit is extracted. Figure 13 shows the ZT figure of merit as a function of the carrier concentration for the $W = 3$ nm thick (110)/[110] (blue lines) and (100)/[110] (black lines) p-type channels. With solid lines we show results for which we only include hole-phonon scattering for the electronic system, and Umklapp-limited scattering for the phononic system. With dashed lines we show results for which in addition we include boundary scattering for both carriers, holes and phonons (hole-SRS for the electronic system, and phonon-boundary scattering for the phononic system). The per-

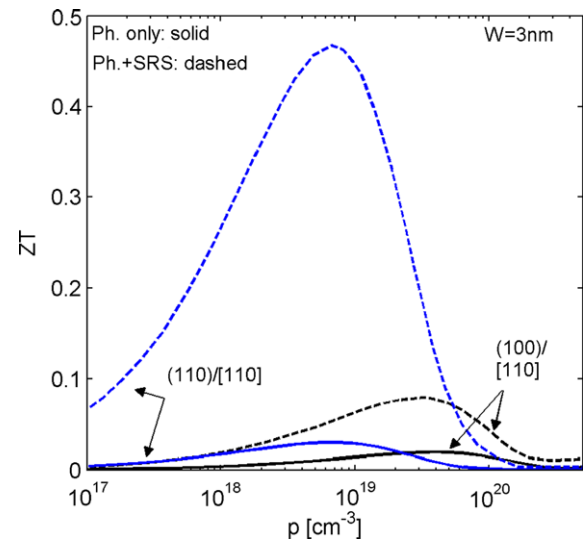


Fig. 13 The ZT figure of merit of p-type UTLs of $W = 3$ nm versus hole density. Blue lines: (110)/[110] channel. Black lines: (100)/[110] channel (as also denoted). Solid lines: hole-phonon scattering-limited power factor and phonon-phonon-limited phonon thermal conductivity is used in the calculation. Dashed lines: phonon plus SRS-limited power factor and phonon-phonon plus phonon-boundary scattering limited phonon thermal conductivity are used in the calculation (Color figure online)

formance advantage of the (110)/[110] channel is evident, reaching room temperature ZT values around $ZT \sim 0.5$, whereas the (100)/[110] channel provides only $ZT \sim 0.1$.

Boundary scattering is beneficial even in the case of the (100) surface because the boundaries affect the phonon system more than the electronic system. We note that we only consider these two orientations in this work because our results indicate that the (110)/[110] channel indicates the best performance compared to all other p-type channels. All others perform very similar to the (100)/[110] channel in terms of power factor and ZT figure of merit [51].

It is interesting to also note the strong dependence of the ZT figure of merit on the density in Fig. 13. This follows from the dependence of the power factor on density as shown in Fig. 8. The ZT for the (110)/[110] channel peaks just before densities of $10^{19}/\text{cm}^3$ and sharply drops as the density deviates from that value. The doping density should, therefore, be precisely controlled in order to achieve high performance. In the case of the (100) surface channels, however, the maximum of ZT appears for densities above $10^{19}/\text{cm}^3$, but it does not peak as sharply as the ZT of the (110) channel. The reason behind this different location of the peaks in density is the lower density of states of the (110) surface, as shown in Fig. 3c. At the same density, the Fermi level is closer to the bands in the (110) channel, which reduces the Seebeck coefficient (shifts to the left as shown in Fig. 8b), and increases the electrical conductivity (also shifts it to the left as shown in Fig. 8a). The result is that the peak of the power factor and ZT appears at lower densities for the (110) channel.

5 Conclusions

In this work we perform atomistic simulations for the electronic, thermal, and thermoelectric properties of ultra-thin Si layers. We couple Linearized Boltzmann theory to: (i) the atomistic $\text{sp}^3\text{d}^5\text{s}^*$ tight-binding model for the electronic properties of the thin layers, and (ii) the modified valence-force-field method for the calculation of the thermal conductivity of the thin layers. We calculate the room temperature electrical conductivity, Seebeck coefficient, power factor, thermal conductivity, and ZT figure of merit of ultra-thin p-type Si layers of thicknesses $W = 3$ nm and 10 nm. We show that their electronic and thermoelectric properties are highly anisotropic, with the (110)/[110] channel indicating the highest performance in terms of the ZT figure of merit.

Acknowledgements The work leading to these results has received funding from the European Community's Seventh Framework Programme under grant agreement no. FP7-263306, and the Austrian Science Fund (FWF), grant P25368-N30.

References

- Hochbaum, A.I., Chen, R., Delgado, R.D., Liang, W., Garnett, E.C., Najarian, M., Majumdar, A., Yang, P.: *Nature* **451**, 163–168 (2008)
- Boukai, A.I., Bunimovich, Y., Kheli, J.T., Yu, J.-K., Goddard, W.A. III, Heath, J.R.: *Nature* **451**, 168–171 (2008)
- Tang, J., Wang, H.-T., Lee, D.H., Fardy, M., Huo, Z., Russell, T.P., Yang, P.: *Nano Lett.* **10**(10), 4279–4283 (2010)
- Li, D., Wu, Y., Fang, R., Yang, P., Majumdar, A.: *Appl. Phys. Lett.* **83**, 3186–3188 (2003)
- Niensch, K., Bachmann, J., Kimling, J., Böttner, H.: *Adv. Energy Mater.* **1**, 713 (2011)
- Hicks, L.D., Dresselhaus, M.S.: *Phys. Rev. B* **47**(24), 16631 (1993)
- Dresselhaus, M., Chen, G., Tang, M.Y., Yang, R., Lee, H., Wang, D., Ren, Z., Fleurial, J.-P., Gagna, P.: *Adv. Mater.* **19**, 1043–1053 (2007)
- Jaworski, C.M., Kulbachinskii, V., Heremans, J.P.: *Phys. Rev. B* **80**, 125208 (2009)
- Neophytou, N., Zianni, X., Kosina, H., Frabboni, S., Lorenzi, B., Narducci, D.: *Nanotechnology* **24**, 205402 (2013)
- Mahan, G.D., Sofo, J.O.: *Proc. Natl. Acad. Sci. USA* **93**, 7436–7439 (1996)
- Neophytou, N., Kosina, H.: *Phys. Rev. B* **83**, 245305 (2011)
- Neophytou, N., Wagner, M., Kosina, H., Selberherr, S.: *J. Electron. Mater.* **39**(9), 1902–1908 (2010)
- Neophytou, N., Kosina, H.: *J. Comput. Electron.* **11**(1), 29–44 (2012)
- Boykin, T.B., Klimeck, G., Oyafuso, F.: *Phys. Rev. B* **69**(11), 115201 (2004)
- Klimeck, G., Ahmed, S., Hansang, B., Kharche, N., Clark, S., Haley, B., Lee, S., Naumov, M., Ryu, H., Saied, F., Prada, M., Korkusinski, M., Boykin, T.B., Rahman, R.: *IEEE Trans. Electron Devices* **54**(9), 2079–2089 (2007)
- Klimeck, G., Ahmed, S., Kharche, N., Korkusinski, M., Usman, M., Prada, M., Boykin, T.B.: *IEEE Trans. Electron Devices* **54**(9), 2090–2099 (2007)
- Neophytou, N., Paul, A., Lundstrom, M., Klimeck, G.: *IEEE Trans. Electron Devices* **55**(6), 1286–1297 (2008)
- Neophytou, N., Paul, A., Klimeck, G.: *IEEE Trans. Nanotechnol.* **7**(6), 710–719 (2008)
- Karamitaheri, H., Neophytou, N., Karami Taheri, M., Faez, R., Kosina, H.: *J. Electron. Mater.* **42**, 2091 (2013)
- Neophytou, N., Klimeck, G., Kosina, H.: *J. Appl. Phys.* **109**, 053721 (2011)
- Neophytou, N., Kosina, H.: *Appl. Phys. Lett.* **99**, 092110 (2011)
- Lee, S., Oyafuso, F., Von Allmen, P., Klimeck, G.: *Phys. Rev. B* **69**, 045316 (2004)
- Buin, A.K., Verma, A., Anantram, M.P.: *J. Appl. Phys.* **104**, 053716 (2008)
- Scheidmantel, T.J., Draxl, C.A., Thonhauser, T., Badding, J.V., Sofo, J.O.: *Phys. Rev. B* **68**, 125210 (2003)
- Yang, M., Chan, V.W.C., Chan, K.K., Shi, L., Fried, D.M., Stathis, J.H., Chou, A.I., Gusev, E., Ott, J.A., Burns, L.E., Fischetti, M.V., Jeong, M.: *IEEE Trans. Electron Devices* **53**(5), 965–978 (2006)
- Tsutsui, G., Saitoh, M., Hiramoto, T.: *IEEE Electron Device Lett.* **26**, 836 (2005)
- Fischetti, M.V., Laux, S.E.: *J. Appl. Phys.* **80**, 2234 (1996)
- Jin, S., Fischetti, M.V., Tang, T.-W.: *J. Appl. Phys.* **102**, 083715 (2007)
- Yamada, T., Ferry, D.K.: *Solid-State Electron.* **38**, 881 (1995)
- Ryu, H.J., Aksamija, Z., Paskiewicz, D.M., Scott, S.A., Lagally, M.G., Knezevic, I., Eriksson, M.A.: *Phys. Rev. Lett.* **105**, 256601 (2010)
- Donetti, L., Gamiz, F., Rodriguez, N., Godoy, A.: *IEEE Electron Device Lett.* **30**(12), 1338 (2009)
- Nishiguchi, N.: *Phys. Rev. B* **54**, 1494 (1996)
- Donetti, L., Gamiz, F., Roldan, J.B., Godoy, A.: *J. Appl. Phys.* **100**, 013701 (2006)
- Buin, A.K., Verma, A., Svizhenko, A., Anantram, M.P.: *Nano Lett.* **8**(2), 760–765 (2008)

35. Ramayya, E.B., Vasileska, D., Goodnick, S.M., Knezevic, I.: J. Appl. Phys. **104**, 063711 (2008)
36. Uchida, K., Takagi, S.: Appl. Phys. Lett. **82**(17), 2916–2918 (2003)
37. Paul, A., Luisier, M., Klimeck, G.: J. Comput. Electron. **9**, 160–172 (2010)
38. Neophytou, N., Klimeck, G.: Nano Lett. **9**(2), 623–630 (2009)
39. Neophytou, N., Kosina, H.: J. Electron. Mater. **41**(6), 1305–1311 (2012)
40. Sui, Z., Herman, I.P.: Phys. Rev. B **48**, 17938–17953 (1993)
41. Karamitaheri, H., Neophytou, N., Pourfath, M., Kosina, H.: J. Comput. Electron. **11**, 14–21 (2012)
42. Nilsson, G., Nelin, G.: Phys. Rev. B **6**, 3777 (1972)
43. Aksamija, Z., Knezevic, I.: Phys. Rev. B **82**, 045319 (2010)
44. Jeong, C., Datta, S., Lundstrom, M.: J. Appl. Phys. **111**, 093708 (2012)
45. Ziman, J.M.: Electrons and Phonons: The Theory of Transport Phenomena in Solids. Clarendon, Oxford (1962)
46. Mingo, N., Broido, D.A.: Nano Lett. **5**, 1221–1225 (2005)
47. Luisier, M.: Phys. Rev. B **86**, 245407 (2012)
48. Donadio, D., Galli, G.: Nano Lett. **10**, 847–851 (2010)
49. Turney, J.E., McGaughey, A.J.H., Amon, C.H.: J. Appl. Phys. **107**, 024317 (2010)
50. Karamitaheri, H., Neophytou, N., Kosina, H.: J. Appl. Phys. **113**, 204305 (2013)
51. Neophytou, N., Kosina, H.: J. Appl. Phys. **112**, 024305 (2012)